PHYSICAL REVIEW MATERIALS **9**, 064603 (2025)

Ab initio thermal conductivity of $Ge_xSn_{1-x}O_2$ alloys

Xiao Zhang and Emmanouil Kioupakis*
Department of Materials Science and Engineering, University of Michigan, Ann Arbor, Michigan 48109, USA

(Received 18 March 2025; accepted 19 May 2025; published 20 June 2025)

Rutile GeO_2 is an emerging ultra-wide band gap semiconductor (UWBG) that has demonstrated excellent potential for applications in power electronic devices. Alloys of rutile SnO_2, a well-established UWBG semiconducting oxide, with GeO_2 are promising for tuning the material properties for applications. The thermal conductivity, in particular, is a key property, which is significantly impacted by alloy disorder, but which is also essential in assessing the operation and degradation of materials in high-power electronic applications. Here, we present first-principles calculations of the thermal conductivity of rutile GeO_2, SnO_2, and their alloys, and quantify the effects of scattering by alloy disorder, temperature, and isotope mass distribution. We show that the relatively high thermal conductivity of the binary compounds is reduced by alloying and isotope disorder. We further assess grain boundary effects via quantifying the impact of phonon mean free path. However, we also find that the room-temperature thermal conductivity of the alloys is still comparable to or surpasses the values for β-Ga_2O_3, an established UWBG semiconducting oxide. Our findings provide a roadmap for the co-design of the thermal properties of rutile $Ge_xSn_{1-x}O_2$ alloys for electronic device applications.

DOI: 10.1103/cgkf-djns

I. INTRODUCTION

SnO_2 is a well-established ultra-wide band gap (UWBG) semiconductor. With a band gap of approximately 3.7 eV and excellent carrier transport capability [1–4], the material has been widely studied for many applications, such as sensors [5,6] and transparent conductors [7–11]. Additionally, GeO_2, which under ambient conditions adopts the same rutile crystal structure as SnO_2, is an emerging UWBG semiconductor that, in recent years, has gained significant attention for power electronics applications [12–14]. It has been predicted to have a potential ambipolar dopability [15,16], high carrier mobilities for both electrons and holes [17], and a high breakdown field due to its ultra-wide electronic band gap [16]. Experimental realizations of high-quality r-GeO_2 have been demonstrated via several different routes [13,18–23]. Possible doping techniques have been explored [24,25] and efficient n-type doping of bulk crystals with Sb^{5+} has been successfully demonstrated above 10^{20} cm^{-3} [26]. Alloying GeO_2 with SnO_2 introduces the possibility of tuning the material properties [27–29], providing an opportunity to develop alloys optimized for specific application needs. The experimental growth of $Ge_xSn_{1-x}O_2$ alloys has been reported using pulsed laser deposition (PLD) [28,29], chemical vapor deposition (CVD) [27], and molecular beam epitaxy (MBE) [30] methods across a range of alloy compositions. Interestingly, it has been demonstrated that the alloys exhibit carrier mobilities that are not very sensitive to composition up to x ∼0.57 [27,29]. This insensitivity indicates that $Ge_xSn_{1-x}O_2$ alloys can maintain favorable electronic transport properties even with significant changes in composition, which is advantageous for device design and manufacturability.

While the electronic properties of $Ge_xSn_{1-x}O_2$ alloys are promising, their thermal conductivities must also be carefully evaluated to ensure their effectiveness in high-power applications. In power electronics, devices must dissipate substantial amounts of heat to maintain stability and prevent degradation over time. A high thermal conductivity enables efficient heat dissipation, which is particularly important for materials expected to function in compact or high-power-density configurations. While both SnO_2 and GeO_2 are known for their high thermal conductivities [31,32], the presence of alloy disorder often leads to significant phonon scatterings and, thus, a corresponding reduction in the thermal conductivity, a phenomenon observed in many other alloy systems [33–37]. Therefore, to assess the potential of $Ge_xSn_{1-x}O_2$ alloys for power electronic applications, it is essential to quantify the effect of alloy disorders on their thermal conductivities.

In this study, we employ first-principles calculations to consistently investigate the lattice thermal conductivity of GeO_2, SnO_2, and $Ge_xSn_{1-x}O_2$ alloys as a function of composition and temperature. Subsequently, we provide a compact model, fitted to *ab initio* data, to describe the temperature- and composition-dependent thermal conductivity of the $Ge_xSn_{1-x}O_2$ alloy. Our findings show that alloying significantly reduces the thermal conductivity compared to the binary compounds. However, even the lowest conductivity value remains similar to β-Ga_2O_3, another UWBG semiconducting oxide. Furthermore, by analyzing the impact of phonon mean free path (MFP) and isotope scattering on thermal properties, we provide insights into the fundamental factors that limit the thermal conductivity of these alloys.

II. COMPUTATIONAL METHODS

First-principles calculations are performed with density functional theory [38,39] and related approaches. Structural

---

[*] Contact author: kioup@umich.edu

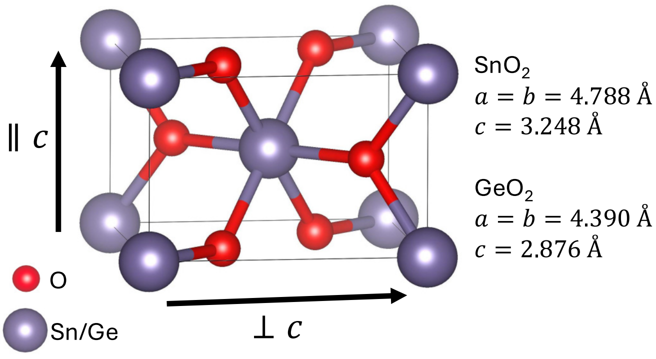

FIG. 1. Primitive unit cell of SnO$_2$ and GeO$_2$. Both materials adopt the rutile structure containing two formula units per unit cell with crystalline direction $a = b$ and a shorter c direction.

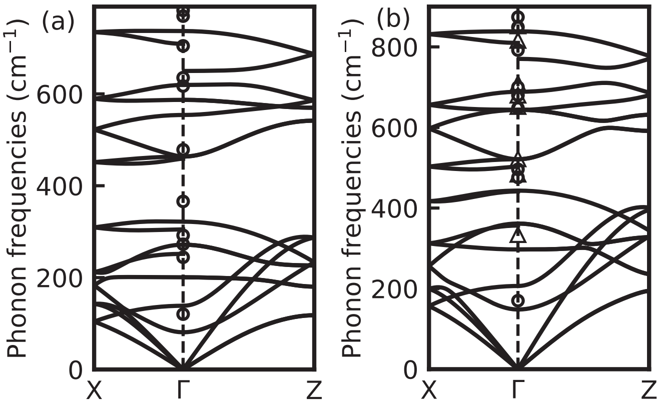

FIG. 2. Phonon dispersion of (a) SnO$_2$ and (b) GeO$_2$ along the $X - \Gamma$ ($\perp c$) and $\Gamma - Z$ ($\parallel c$) high-symmetry path of the first Brillouin zone. Our results are in good agreement with theoretical calculations from Ref. [1] for SnO$_2$ and Ref. [32] for GeO$_2$. Good agreement is also seen compared to experimental measurements for SnO$_2$ (Ref. [50]) and GeO$_2$. (Circles: Ref. [51]; Triangles: Ref. [52].)

relaxations are performed with the Quantum Espresso (QE) [40,41] package, using norm-conserving pseudopotentials [42] and the local density approximation for the exchange-correlation functional [43,44]. The structure of rutile GeO$_2$ and rutile SnO$_2$ is shown in Fig. 1. For Ge and Sn, the 3d and 4d electrons are included in the valence, respectively, to ensure accurate phonon frequencies. Plane-wave energy cutoffs of 140 Ry are used to ensure the convergence of the total energy within 1 meV/atom. The unit cells are relaxed until the forces on the atoms are less than 5×10^{-5} Ry/Bohr, and the total stresses on the unit cells are less than 5×10^{-6} Ry/Bohr^3. The relaxed lattice constants are $a = b = 4.788$ Å and $c = 3.248$ Å for SnO$_2$; $a = b = 4.390$ Å and $c = 2.876$ Å for GeO$_2$, both in excellent agreement with previous theoretical calculations [1,32]. Density functional perturbation theory [45] is used to evaluate vibrational properties within the harmonic approximation to obtain the second-order (harmonic) force constants, implemented in the QE package. Phonon frequencies are evaluated on a Brillouin zone (BZ) sampling grid of $6 \times 6 \times 9$, therefore producing the second-order force constants corresponding to a $6 \times 6 \times 9$ supercell.

The key theory and ingredients to evaluate the lattice thermal conductivity are shown in Appendix A 1. To evaluate the lattice thermal conductivity, third-order anharmonic force constants are required, which are obtained through finite-difference approach with atomic displacements using $4 \times 4 \times 4$ supercells of the primitive unit cell. Interactions up to fifth-nearest neighbors are considered. The structures, force constants, and Born effective charges are supplied to the almaBTE [46] code to solve the phonon Boltzmann transport equation (BTE) in order to evaluate the thermal conductivity of GeO$_2$ and SnO$_2$. To evaluate thermal conductivities of the alloys, the virtual crystal approximation is used, which takes the arithmetic averages [46]: $\phi_{VC} = \sum_i x_i \phi_i$, where ϕ_{VC}, ϕ_i, and i are the physical properties (lattice constants, atomic coordinates, force constants) of the virtual crystal, the end compound, and the mole fraction of the end compound, respectively. While in principle, accurate modeling of alloy systems require consideration of the evolution of bonding, local structures, etc, which is better represented by, e.g., special quasi-random structures [47], the very large cell size and the lack of symmetry make it practically unfeasible to evaluate particularly third-order force constants in these structures. Therefore, in our work, we investigate the effect of alloying by considering random mass disorders throughout the calculations in this article. The average atomic mass with the natural isotope distribution [48] of Ge (72.64 amu) and Sn (118.71 amu) are used. The effect of isotope mass disorder is examined separately for the binary compounds using ShengBTE [49]. The isotopes considered according to natural isotope distribution [48,49] are for Ge: Ge^{70} (20.5%), Ge^{72} (27.4%), Ge^{73} (7.8%), Ge^{74} (36.5%), and Ge^{76} (7.8%). For Sn: Sn^{112} (0.97%), Sn^{114} (0.65%), Sn^{115} (0.36%), Sn^{116} (14.7%), Sn^{117} (7.7%), Sn^{118} (24.3%), Sn^{119} (8.6%), Sn^{120} (32.4%), Sn^{122} (4.6%), and Sn^{124} (5.6%). A BZ sampling grid of $16 \times 16 \times 24$ is used consistently to evaluate the thermal conductivities of SnO$_2$, GeO$_2$, and the alloys. The thermal conductivity is converged with 5% and a set of convergence tests with respect to various computational parameters can be found in Appendix A 2.

III. PHONON PROPERTIES

The calculated phonon dispersion relations for rutile SnO$_2$ and GeO$_2$ along the $\perp c$ and $\parallel c$ directions are shown in Fig. 2. The calculated phonon frequencies are in good agreement with previous calculations [1,32] and experimental measurements [50–52]. Overall, the phonon frequencies of GeO$_2$ are higher than SnO$_2$, which is attributed to the lighter atomic mass of Ge. We further evaluate the sound velocity based on the slope of the acoustic phonon branches near the Γ-point, as shown in Table I. Our calculated sound velocities agree well with the reported values in the literature [17,53,54]. We find the sound velocity to be generally larger in GeO$_2$ by a factor from $1.22 \sim 1.38$. The ratio is consistent with the inverse square root of the atomic mass of Ge and Sn ($(m_{\mathrm{Ge}}/m_{\mathrm{Sn}})^{-1/2} = 1.28$). The consistency is expected as the acoustic phonons are dominated by the heavy atoms, whose group velocity is inversely dependent on the square root of their atomic mass [55]. The higher speed of sound in GeO$_2$

TABLE I. Sound velocities (in km/s) for the LA (v_{LA}) and TA (v_{TA}) modes along the $\perp c$ and $\parallel c$ directions, and directional averages in SnO_2 and GeO_2. Our calculated values agree well with theoretical study in Ref. [17], as well as experimental characterizations listed in the Table from Ref. [53] for SnO_2 (directionally averaged) and Ref. [54] for GeO_2.

Sound velocity	$v_{\mathrm{TA}}, \perp c$	$v_{\mathrm{TA}}, \parallel c$	$v_{\mathrm{LA}}, \perp c$	$v_{\mathrm{LA}}, \parallel c$	$v_{\mathrm{TA}}^{\mathrm{ave}}$	$v_{\mathrm{LA}}^{\mathrm{ave}}$	$v_{\mathrm{TA}}, \perp c$ (Expt.)	$v_{\mathrm{TA}}, \parallel c$ (Expt.)	$v_{\mathrm{LA}}, \perp c$ (Expt.)	$v_{\mathrm{LA}}, \parallel c$ (Expt.)
SnO_2	4.41	3.50	5.78	7.75	4.10	6.44	3.79		6.75	
GeO_2	5.65	4.86	7.09	9.48	5.39	7.89	5.072	6.415	7.328	9.770

contributes to its higher thermal conductivity, as confirmed by our subsequent calculations in Sec. IV.

We further analyze the relaxation times of the phonons as a function of phonon frequencies, as shown in Fig. 3. For both SnO_2 and GeO_2, the relaxation times of the acoustic phonons decrease over three orders of magnitude from 10^{-9}s to 10^{-12}s with increasing phonon frequency from 0 to 400 cm^{-1}, while the relaxation times for the optical phonons are approximately on the order of 10^{-12}s, in general. Therefore, the low-frequency acoustic modes are expected to play a significant role in enabling high thermal conductivity for both binary compounds. However, alloying significantly increases the phonon scattering in $Ge_xSn_{1-x}O_2$, resulting in a much steeper decrease of the phonon relaxation times with increasing frequency. This effect is particularly pronounced in the frequency range below 400 cm^{-1}, where phonons in the alloy exhibit significantly lower relaxation times compared to the binary compounds. The substantial decrease in phonon relaxation times for the alloy suggests a notably lower thermal conductivity, which we demonstrate in the following section.

IV. THERMAL CONDUCTIVITY

A. Thermal conductivity with respect to temperature and alloy composition

The calculated temperature-dependent thermal conductivity of binary SnO_2 and GeO_2 (Fig. 4) is in good agreement with experimental measurements for both materials [31,32]. For both materials, the dependence of their thermal conductivity can be described by the following equation:

$$\kappa(T) = \left[\frac{1}{\kappa_1}e^{-T_1/T} + \frac{1}{\kappa_2}e^{-T_2/T}\right]^{-1}. \tag{1}$$

In this equation, κ_1 and κ_2 are in units of thermal conductivities, and T_1 and T_2 are in units of temperatures. The model assumes a similar two-mode model illustrated in Ref. [17] for electron mobility with the two κ's and T's representing the contribution to thermal conductivity of the two different modes. The values of these parameters fitted from a full set of temperature- and composition-dependent models can be found in Table II. Figure 4 shows that the fit well describes the temperature dependence of the thermal conductivity for

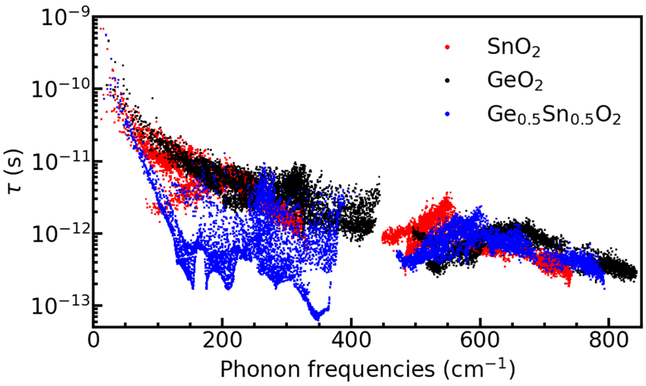

FIG. 3. Phonon lifetimes due to a combination of three-phonon scattering and alloy/isotope mass-scattering processes for SnO_2, GeO_2, and $Ge_{0.5}Sn_{0.5}O_2$. Phonon lifetimes generally decrease with increasing phonon frequencies and are similar for the two binary compounds. A much steeper decrease is observed for the alloy, particularly for the low-frequency acoustic phonons due to alloy mass disorder.

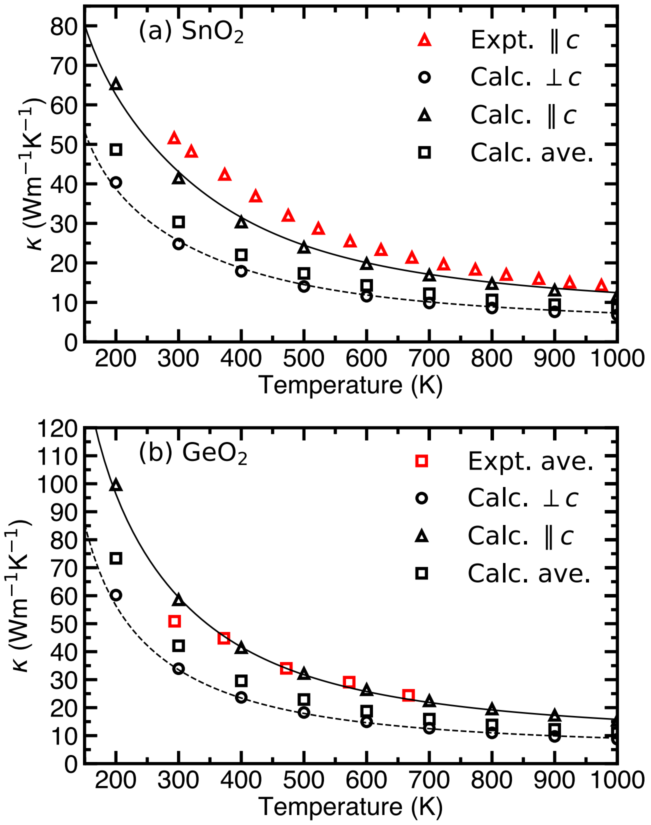

FIG. 4. Temperature-dependent thermal conductivities of (a) SnO_2 and (b) GeO_2, reported both along the $\parallel c$ and $\perp c$ directions, as well as a directional average for comparison to polycrystalline samples. Fitted curves according to a two-mode model [Eq. (1)] and parameters from Table II are shown as dashed and solid lines for $\perp c$ and $\parallel c$ directions. Good agreement is achieved compared to experimental measurements, both for SnO_2 [31] (single crystal, $\parallel c$) and GeO_2 [32] (polycrystal).

TABLE II. Fitted values for the temperature- and alloy-composition-dependent thermal conductivity model of Eq. (3). Parameters $\kappa_{1,\mathrm{Sn}}$, $\kappa_{1,\mathrm{Ge}}$, $\kappa_{2,\mathrm{Sn}}$, $\kappa_{2,\mathrm{Ge}}$, and κ' are reported in units of thermal conductivity ($\mathrm{Wm^{-1}K^{-1}}$), parameters $T_{1,\mathrm{Sn}}$, $T_{1,\mathrm{Ge}}$, $T_{2,\mathrm{Sn}}$, $T_{2,\mathrm{Ge}}$, and T' are in units of temperature (K), while α is a dimensionless parameter. The fitted values are also used to describe temperature dependence for the end compounds [Eq. (1)], as well as composition dependence at 300 K [Eq. (2)].

	α	$\kappa_{1,\mathrm{Sn}}$	$\kappa_{2,\mathrm{Sn}}$	$T_{1,\mathrm{Sn}}$	$T_{2,\mathrm{Sn}}$	$\kappa_{1,\mathrm{Ge}}$	$\kappa_{2,\mathrm{Ge}}$	$T_{1,\mathrm{Ge}}$	$T_{2,\mathrm{Ge}}$	κ'	T'
$\perp c$	0.686	16.6	3.59	176	1175	18.6	4.85	231	1123	5.99	58.0
$\parallel c$	0.666	34.3	6.14	129	1091	37.7	7.88	197	1118	7.06	54.9

both materials of the entire temperature range. GeO_2 shows a higher thermal conductivity for both modes. Though the two-mode model cannot be linked directly to phonon frequencies, they can be understood by representing two phonon transport channels, where the contribution from low frequency acoustic phonons are activated at low temperatures, and high-frequency optical phonons activated at higher temperatures. While the temperature of the high-energy modes are similar between the two materials, the temperature of the low-energy mode is higher in GeO_2. This trend is consistent with the cations dominating the acoustic modes and, because Ge is lighter than Sn, GeO_2 exhibits higher acoustic-mode frequencies. The oxygen anions, meanwhile, contribute primarily to the optical modes.

We next present the calculated thermal conductivities of the $Ge_xSn_{1-x}O_2$ alloys at room temperature in Fig. 5. The thermal conductivity of the alloy decreases significantly as the composition deviates from the pure compounds. At 10% Ge or Sn content, the thermal conductivity drops to 53% and 49% of that of pure SnO_2 and GeO_2, respectively. The thermal conductivities across alloy compositions from $x = 0.1$ to $x = 0.9$ are reduced within a factor of 0.57 from the values at $x = 0.1$ and $x = 0.9$. The composition-dependent thermal conductivity at room temperature is described by the following equation:

$$\kappa^{300K}(x) = \left[\frac{(1-x)^\alpha}{\kappa^{300K}_{\mathrm{SnO_2}}} + \frac{x^\alpha}{\kappa^{300K}_{\mathrm{GeO_2}}} + \frac{[x(1-x)]^\alpha}{\kappa'_{300K}}\right]^{-1}. \quad (2)$$

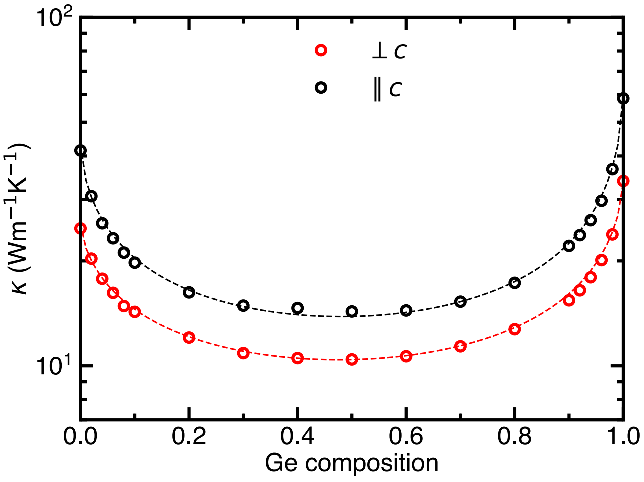

FIG. 5. Calculated thermal conductivity of $Ge_xSn_{1-x}O_2$ alloys at room temperature (300 K) as a function of alloy composition and crystallographic orientation, as well as fitted curves (dashed) from the model described by Eq. (2), and parameters shown in Table II. The thermal conductivity of the alloy is significantly reduced by alloy scattering, but even the lowest value remains comparable to that of Ga_2O_3 [11–15 $\mathrm{Wm^{-1}K^{-1}}$ ($\perp c$), 15–20 $\mathrm{Wm^{-1}K^{-1}}$ ($\parallel c$)] [31].

In this equation, κ'_{300K} is a bowing parameter used to model the effect of alloy disorder [33,34] and α is a measure of the decay of the thermal conductivity close to the two binary compounds. The fitted values of the parameters are $\alpha = 0.686$ and 0.666 for the $\perp c$ and $\parallel c$ directions, while the bowing at 300 K is obtained as $\kappa'_{300K} = 7.27\ \mathrm{Wm^{-1}K^{-1}}$ for the $\perp c$ and $\kappa'_{300K} = 8.48\ \mathrm{Wm^{-1}K^{-1}}$ for the $\parallel c$ directions (see Table II). Comparing the result of the thermal conductivity of the $Ge_{0.5}Sn_{0.5}O_2$ alloy to β-Ga_2O_3, we find that both the in-plane ($\perp c$) and out-of-plane ($\parallel c$) thermal conductivity of the alloy are comparable to that of the pure Ga_2O_3 [11–15 $\mathrm{Wm^{-1}K^{-1}}$ ($\perp c$), 15–20 $\mathrm{Wm^{-1}K^{-1}}$ ($\parallel c$)] [31]. Our findings suggest that, despite the significant reduction in their thermal conductivity due to alloying, the heat dissipation in $Ge_xSn_{1-x}O_2$-based devices is comparable to that of Ga_2O_3-based devices.

Next, we present the temperature- and composition-dependent thermal conductivity of $Ge_xSn_{1-x}O_2$ alloys in Fig. 6; see full tabulated data in the Supplemental Material [56]. The thermal conductivity is fitted with the following equation, which combines the effects of temperature and composition dependence:

$$\begin{aligned}\kappa(x,T) = \Bigg\{&(1-x)^\alpha\left[\frac{1}{\kappa_{1,\mathrm{Sn}}}e^{-T_{1,\mathrm{Sn}}/T} + \frac{1}{\kappa_{2,\mathrm{Sn}}}e^{-T_{2,\mathrm{Sn}}/T}\right]\\ &+ x^\alpha\left[\frac{1}{\kappa_{1,\mathrm{Ge}}}e^{-T_{1,\mathrm{Ge}}/T} + \frac{1}{\kappa_{2,\mathrm{Ge}}}e^{-T_{2,\mathrm{Ge}}/T}\right]\\ &+ \frac{[x(1-x)]^\alpha}{\kappa'}e^{-T'/T}\Bigg\}^{-1}.\end{aligned} \quad (3)$$

In this equation, the parameters $\kappa_{1,\mathrm{Sn}}$, $\kappa_{1,\mathrm{Ge}}$, $\kappa_{2,\mathrm{Sn}}$, $\kappa_{2,\mathrm{Ge}}$, and κ' are in units of thermal conductivity, parameters $T_{1,\mathrm{Sn}}$, $T_{1,\mathrm{Ge}}$, $T_{2,\mathrm{Sn}}$, $T_{2,\mathrm{Ge}}$, and T' are in units of temperature, while α is a dimensionless exponent. For $x = 0$ and $x = 1$, Eq. (3) reduces to Eq. (1), as only the SnO_2- or GeO_2-related terms are nonzero. At a specific temperature, Eq. (3) reduces to Eq. (2), as each term related to temperature reduces to a constant value in units of thermal conductivity. The values of the fitted parameters are listed in Table II, and the fitted equations are plotted as a 2D heat map with isolines, shown in Fig. 7. In the entire temperature and composition range, the maximum difference between the fitted values and calculated values is 7.2% and 6.8% in the $\perp c$ and $\parallel c$ directions, respectively. In the case of a nearly equimolar alloy ($x = 0.5$), the significant reduction of the thermal conductivity due to strong

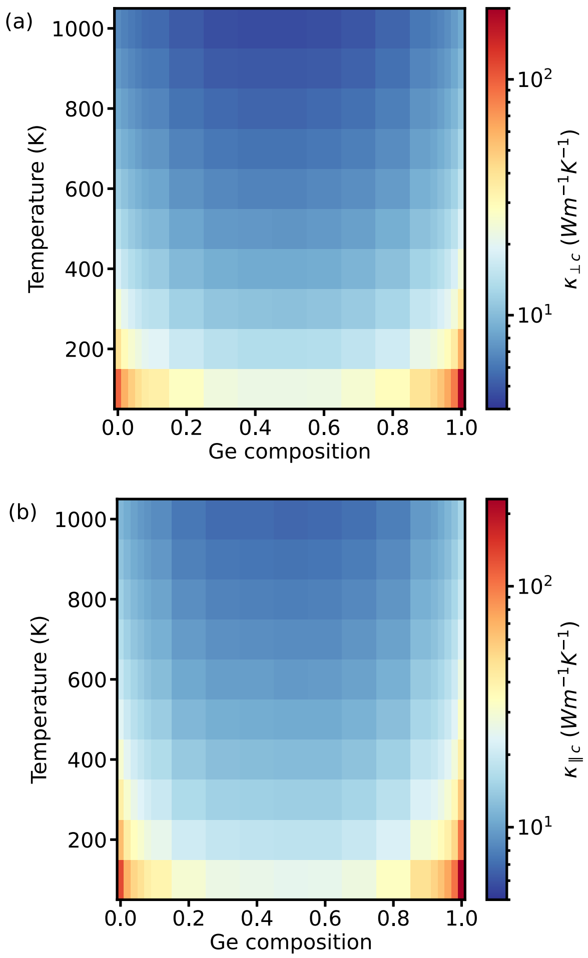

FIG. 6. Thermal conductivity of SnO_2 and GeO_2 alloys as a function of alloy composition and temperature, along the (a) $\perp c$ and (b) $\parallel c$ directions. The significant reduction of thermal conductivity in the alloys suggests strong alloy scattering across the entire temperature range investigated. (See full tabulated data in the Supplemental Material [56].)

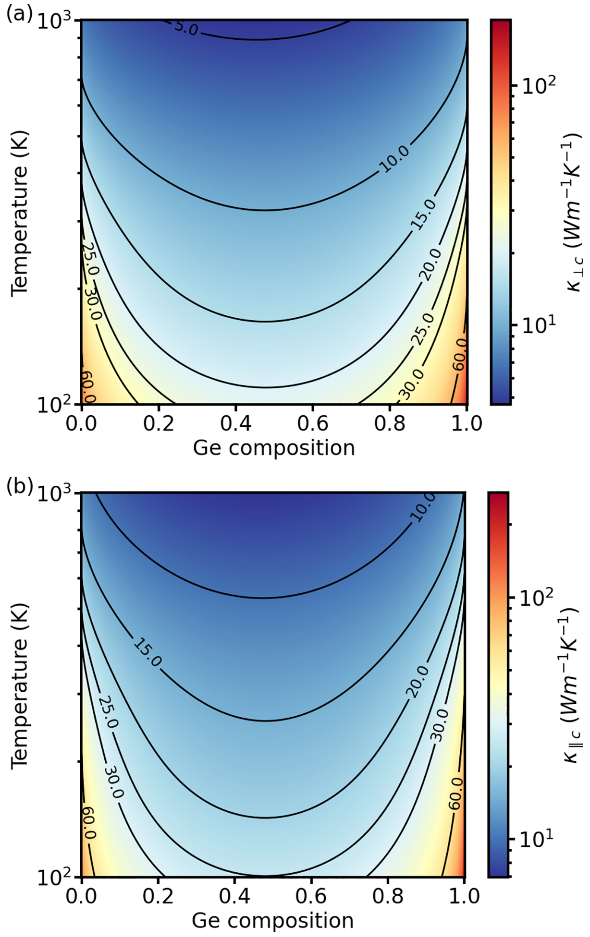

FIG. 7. Plot of the thermal conductivity as a function of Ge composition and temperature with Eq. (3) and the fitted parameters illustrated in Table II, as well as contour lines to demonstrate the values. The maximum variation of the values from the calculated ones in Fig. 6 is 7.2% and 6.8% in the $\perp c$ and $\parallel c$ directions, respectively.

alloy disorder renders a weak dependence when temperature is further considered. For example, the thermal conductivity along $\perp$ c for the equimolar alloy reduces from 22 $Wm^{-1}K^{-1}$ to 5.9 $Wm^{-1}K^{-1}$ from 100 K to 1000 K, while for pure GeO_2, a reduction over an order of magnitude is seen from 187 $Wm^{-1}K^{-1}$ to 8.7 $Wm^{-1}K^{-1}$. This trend of strong alloy disorder dominating over the temperature dependence is also observed in III-V alloys, such as AlGaN [35].

B. Impact of phonon mean free path and isotope scattering

We further analyze the dependence of the thermal conductivity on the mean free path of the phonons to provide insight on the effect of scattering by grain boundaries in polycrystalline samples. In Fig. 8, we show the cumulative thermal conductivity at room temperature (300 K) evaluated within the relaxation time approximation, including only those phonons that have a mean free path up to the specified value. This analysis offers an evaluation of the fundamental upper limit of the lattice thermal conductivity for a given average grain size. We find a sharp increase of the phonon-limited thermal conductivity as the phonon mean free path increases from 10 nm to 100 nm, which is consistent with a previous theoretical study for GeO_2 [32]. In general, it is expected that high-quality crystals result in reduced scattering by grain boundaries, therefore benefiting thermal conductivity. In Table III, we list the values of the phonon mean free path required to achieve 80% of the ideal thermal conductivity for SnO_2, GeO_2, and the equimolar alloy in the $\perp c$ and $\parallel c$ directions. Our calculations quantify the grain sizes required to achieve desired theoretical thermal conductivity limits for efficient thermal management.

Due to the different masses of the various isotopes of a given atomic species, isotope mass disorder is expected to affect the thermal conductivity. We quantify the effects of isotope scatterings in SnO_2 and GeO_2, and we uncover a stronger effect of isotope scattering in GeO_2. In Fig. 9, we show the effect of isotope scattering on thermal conductivity by plotting the ratio of thermal conductivity evaluated with the average isotope mass, including mass disorder, to that of the isotope pure material considering the three-most-abundant species as a function of temperature for both SnO_2 and GeO_2.

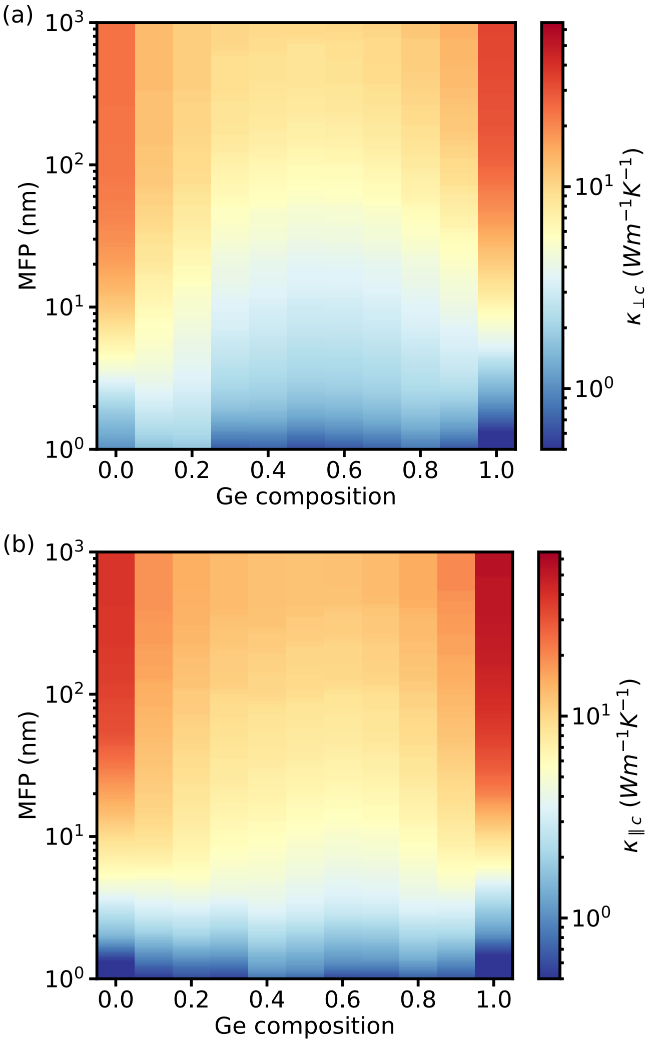

FIG. 8. Cumulative thermal conductivities of $Ge_xSn_{1-x}O_2$ at 300 K as a function of Ge content and the mean free path of the phonon projected to the respective directions for the (a) $\perp c$ and (b) $\parallel c$ directions. The thermal conductivity is strongly affected by the mean free path in the region of 10–100 nm. (See full tabulated data in the Supplemental Material [56].)

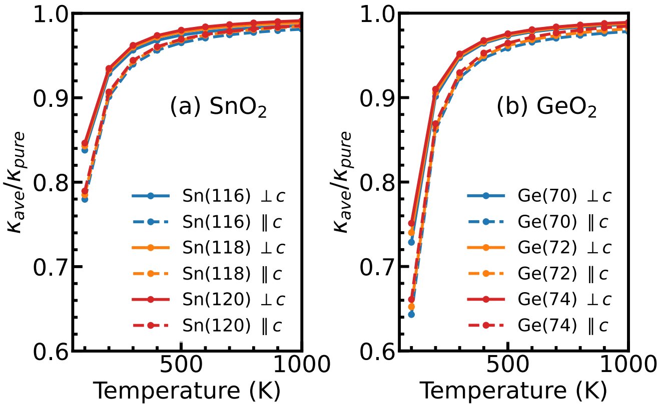

FIG. 9. Ratio of the thermal conductivity of (a) SnO_2 and (b) GeO_2 evaluated with the average atomic mass considering isotope mass disorder (κ_{ave}) as compared to that with a pure isotope (κ_{pure}). The three-most-abundant isotopes are considered for each material. For both materials, isotope scattering has a stronger impact on the thermal conductivity at low temperatures and along the $\parallel c$ direction.

This ratio provides a measure of how the scattering induced by isotope mass disorder affects thermal transport across different temperatures. SnO_2 shows a more modest reduction across all temperatures compared to GeO_2. At low temperatures (e.g., 100 K), isotope scattering significantly reduces the thermal conductivity of GeO_2 by 26% in the $\perp c$ and 36% in the $\parallel c$ directions, compared to a more-moderate reduction in SnO_2 of 16% in the $\perp c$ and 22% in the $\parallel c$. At higher temperature, such as room temperature (300 K), the impacts of isotope scattering are less significant: Isotope mass disorder is responsible for a reduction of thermal conductivity by 6% in the $\perp c$ and 8% in the $\parallel c$ directions for GeO_2, and by 4% in the $\perp c$ and 6% in the $\parallel c$ directions for SnO_2. As temperature further increases, the relative impact of isotope mass disorder on phonon transports decreases as the ratio gradually approaches unity. These findings provide insight into the fundamental limitations on thermal conductivity in GeO_2-based materials, particularly at lower temperatures.

TABLE III. Phonon mean free path (in nm) required for the thermal conductivity to reach 80% of the ideal value for SnO_2, GeO_2 and $Ge_{0.5}Sn_{0.5}O_2$ at 300 K. For all cases, achieving 80% of the ideal value of thermal conductivity requires grain sizes above 100 nm.

Compound	SnO_2	GeO_2	$Ge_{0.5}Sn_{0.5}O_2$
$\perp c$	176	125	354
$\parallel c$	110	160	369

V. CONCLUSION

In this study, we provide a comprehensive analysis of the thermal conductivity of GeO_2, SnO_2, and their alloys utilizing first-principles calculations. Our findings reveal that alloying significantly reduces thermal conductivity due to enhanced phonon scattering, particularly for the acoustic phonon modes. Despite this reduction, the thermal conductivity of the alloys remains comparable with β-Ga_2O_3. We also produced a complete analytical model that fits the first-principles thermal conductivity data of $Ge_xSn_{1-x}O_2$ alloys across various compositions and temperatures. We found a two-mode model to well-describe the temperature- and composition-dependent thermal conductivity of the alloy, offering valuable predictive power for optimizing alloy design.

Our analysis further shows that polycrystalline samples with grain sizes less than 100 nm reduce the phonon mean free path and, therefore, reduce the thermal conductivity. The influence of Ge and Sn isotopes scattering is found to be considerable at low temperatures, and becomes less dominant as temperature increases. We find isotope mass disorder to reduce the thermal conductivity of the binaries by 5–8% at room temperature, providing insights into the fundamental limitations of thermal conductivity in GeO_2-based materials.

Our findings provide a fundamental understanding of the alloy-, phonon-, and isotope-disorder-limited thermal conductivity in $Ge_xSn_{1-x}O_2$ alloys as a function of composition and temperature, and offer guidance for the co-design of these materials for high-power electronic applications, where both tunable electronic properties and efficient heat dissipation are essential.

ACKNOWLEDGMENTS

This material is based upon work supported by the National Science Foundation under Grant No. 2328701 and is supported in part by funds from federal agency and industry partners, as specified in the Future of Semiconductors (FuSe) program. Computational resources were provided by the National Energy Research Scientific Computing Center, which is supported by the Office of Science of the U.S. Department of Energy under Contract No. DE-AC02-05CH11231.

DATA AVAILABILITY

Data that are not openly available are available upon reasonable request from the authors.

APPENDIX

1. Theoretical approach for evaluating thermal conductivity

In this section, we briefly lay out the theoretical framework of evaluating thermal conductivity. We show the key equations and concepts, and refer to Ref. [57], Ref. [49], and Ref. [46] for a full description of the theory. The lattice thermal conductivity of a material can be expressed by an integral over the Brillouin zone for phonons involving their lifetimes [57]:

$$\kappa = \frac{1}{k_B T^2} \sum_{\alpha} \int n_\lambda (n_\lambda + 1)(\hbar\omega_\lambda)^2 v_\lambda^2 \tau_\lambda \frac{d\mathbf{q}}{(2\pi)^3}. \tag{A1}$$

In Eq. (A1), k_B is the Boltzmann constant, T is the temperature, λ is the phonon mode, and n_λ is the Bose-Einstein occupation factor for the phonons. $\hbar\omega_\lambda$ and v_λ are the energies and group velocities of the phonons, respectively. The phonon properties within the harmonic approximation (second order) are well-established with the density functional perturbation theory [45]. τ_λ represents the relaxation time of the phonons due to scattering events, which is obtained through solving the phonon Boltzmann's transport equation by considering several different scattering mechanisms including three phonon scattering (τ_{3ph}), scattering due to alloy mass disorder, and isotope mass disorder ($\tau_{m.d.}$). The former is obtained via evaluating the third order anharmonic force constants. The third-order force constants characterize the phonon-phonon scattering processes beyond the harmonic approximation, and are obtained through specifically displacing atoms in a supercell and evaluating the force acting on the atoms with the displacement present, as illustrated by Ref. [49]:

$$\Phi_{ijk}^{\alpha\beta\gamma} = \frac{\partial^3 E}{\partial r_i^\alpha \, \partial r_j^\beta \, \partial r_k^\gamma} \simeq \frac{1}{2h}\left[\left.\frac{\partial^2 E}{\partial r_j^\beta \, \partial r_k^\gamma}\right|_{r_i^\alpha=h} - \left.\frac{\partial^2 E}{\partial r_j^\beta \, \partial r_k^\gamma}\right|_{r_i^\alpha=-h}\right] \simeq \frac{1}{4h^2}\big[-F_k^\gamma\big(r_i^\alpha=h, r_j^\beta=h\big) + F_k^\gamma\big(r_i^\alpha=h, r_j^\beta=-h\big) + F_k^\gamma\big(r_i^\alpha=-h, r_j^\beta=h\big) - F_k^\gamma\big(r_i^\alpha=-h, r_j^\beta=-h\big)\big]. \tag{A2}$$

In the equation, $\Phi_{ijk}^{\alpha\beta\gamma}$ is the third-order force constant, where ijk are indices for atoms and $\alpha\beta\gamma$ are indices for Cartesian directions. The equation relates the third-order force constants to the forces acting on single atoms via a finite difference framework, with F being the forces on a specific atom in the presence of a small displacement h of two other atoms. To prevent the extensive computational resources needed to evaluate thousands of supercells, symmetry and a cutoff of nearest neighbor are often applied. In our case, we show a convergence of the nearest neighbor included in the next section, and the production calculations require a total number of 220 384-atom supercells to be evaluated in order to obtain the third-order force constants.

The third-order force constants are used to evaluate three-phonon scattering rates by considering three phonons by 1) satisfying momentum conservation: $\mathbf{q}'' = \mathbf{q}' + \mathbf{q} + \mathbf{Q}$, where $\mathbf{q}'s$ are phonon wave vectors and $\mathbf{Q}$ being a reciprocal lattice vector, and 2) satisfying energy conservation $\omega_\lambda + \omega_{\lambda'} = \omega_{\lambda''}$. The scattering matrix element of a three-phonon scattering process is given by

$$V_{\lambda\lambda'\lambda''} = \sum_{i \in \text{u.c.}} \sum_{j,k} \Phi_{ijk} \frac{e_\lambda(i) e_{\pm\lambda'}(j) e_{-\lambda''}(k)}{\sqrt{M_i M_j M_k}}, \tag{A3}$$

where the plus and minus signs represent the phonon emission and absorption process, and e's represent the phonon eigenfunctions of state λ. With the matrix elements, the scattering rate for a three-phonon scattering process is given by

$$\Gamma_{\lambda\lambda'\lambda''}^{+} = \frac{\hbar\pi}{4} \frac{(n' - n'')\delta(\omega + \omega' - \omega'')}{\omega\omega'\omega''} |V_{\lambda\lambda'\lambda''}^{+}|^2, \tag{A4}$$

$$\Gamma_{\lambda\lambda'\lambda''}^{-} = \frac{\hbar\pi}{4} \frac{(n' + n'' + 1)\delta(\omega - \omega' - \omega'')}{\omega\omega'\omega''} |V_{\lambda\lambda'\lambda''}^{-}|^2. \tag{A5}$$

Summing over all allowed processes for each phonon λ by the other two (λ', λ'') yields the total scattering rate, whose inverse gives the relaxation time $\tau_{\lambda,3ph}$. To further include the effect of alloying and isotopes, a mass disorder term is present to capture the scattering between phonons and random masses in the alloy (or isotopically mixed) system, as illustrated in Ref. [46]:

$$\tau_{\lambda,\text{m.d.}}^{-1} = \frac{\pi\omega_\lambda^2}{2} \sum_{\lambda',i} \frac{\sigma^2(m_i)}{\langle m_i \rangle^2} \left| \sum_{\alpha} \big[e_\lambda^\alpha(i)\big]^* e_{\lambda'}^\alpha(i) \right|^2 \delta(\omega_\lambda - \omega_{\lambda'}). \tag{A6}$$

The equation considers the harmonic phonons, but accounts for their scattering due to mass disorder characterized by the mean ($\langle m_i \rangle^2$) and standard deviation ($\sigma^2(m_i)$) of the

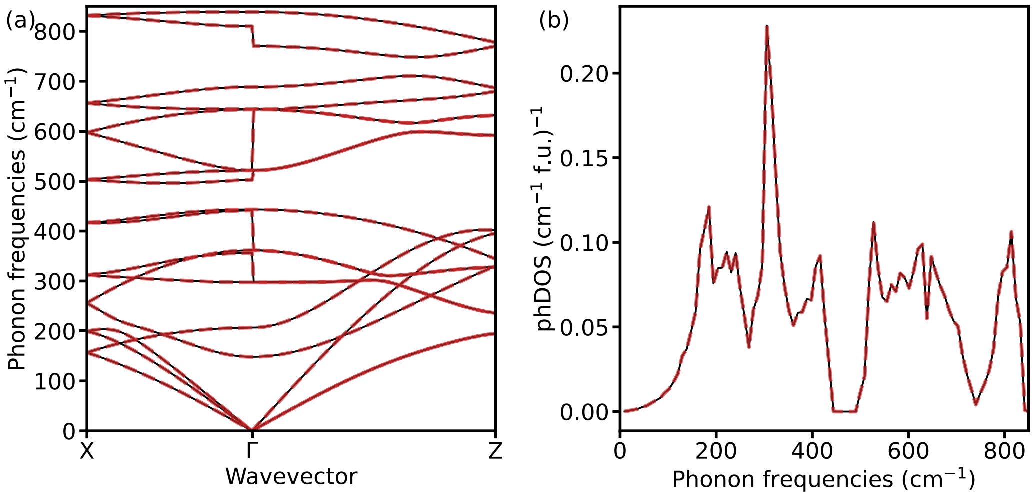

FIG. 10. Calculated phonon properties of GeO_2 with 4 × 4 × 6 (solid black) and 6 × 6 × 9 (dashed red) BZ sampling. (a) shows the phonon dispersion relationship and (b) shows the phonon density of states. No sizable difference is seen between the two sampling grids.

masses on a particular atomic site i, caused by the mass difference from alloying and isotopes. The total phonon relaxation times are, therefore, obtained following the Matthiessen rule, i.e., $\tau_{\lambda}^{-1} = \tau_{\lambda,3ph}^{-1} + \tau_{\lambda,m.d.}^{-1}$. Subsequently, the relaxation times allow an iterative solution of the phonon Boltzmann's transport equation, and compute the thermal conductivity in Eq. (A1).

2. Convergence of the thermal conductivity

In this section, we show the convergence test of the calculated thermal conductivity with respect to several computational parameters. Due to the similarity of the two binaries in their structure, we performed the convergence test only with GeO_2. The main convergence parameters we investigated is the grid of the second-order force constant calculations, the supercell size for the third-order force constants, the number of nearest neighbor considered in the supercell, and the sampling grid of the Brillouin zone for solving the Boltzmann's transport equations.

We first show that the phonon properties remain consistent when changing from a Brillouin zone sampling of 4 × 4 × 6 and then increased to a sampling of 6 × 6 × 9. The maximum difference of the phonon frequencies is 1.3%, and the resulting difference in the thermal conductivity evaluated by solving the Boltzmann's transport equation on a 16 × 16 × 24 grid remains within 0.3%. Therefore, we conclude that further convergence of the second-order force constant is not necessary, and we show the results obtained with the more converged 6 × 6 × 9 grid in the main text. Figure 10 shows that the calculated phonon dispersion relationship and the phonon density of states do not show any sizable differences between a sampling of 4 × 4 × 6 and a sampling of 6 × 6 × 9.

In addition, we tested the convergence of the thermal conductivity evaluated with different supercell sizes. Including up to the third nearest neighbor, the calculated thermal conductivity of GeO_2 at 300 K changes by 1% along both the $\perp c$ and $\parallel c$ directions when increasing from 3 × 3 × 3 to 4 × 4 × 4 supercell, and further by 0.2% when increased to 5 × 5 × 5 supercell. Due to the large change in the computational cost when increasing supercell size, we evaluate the third-order force constant using 4 × 4 × 4 supercell.

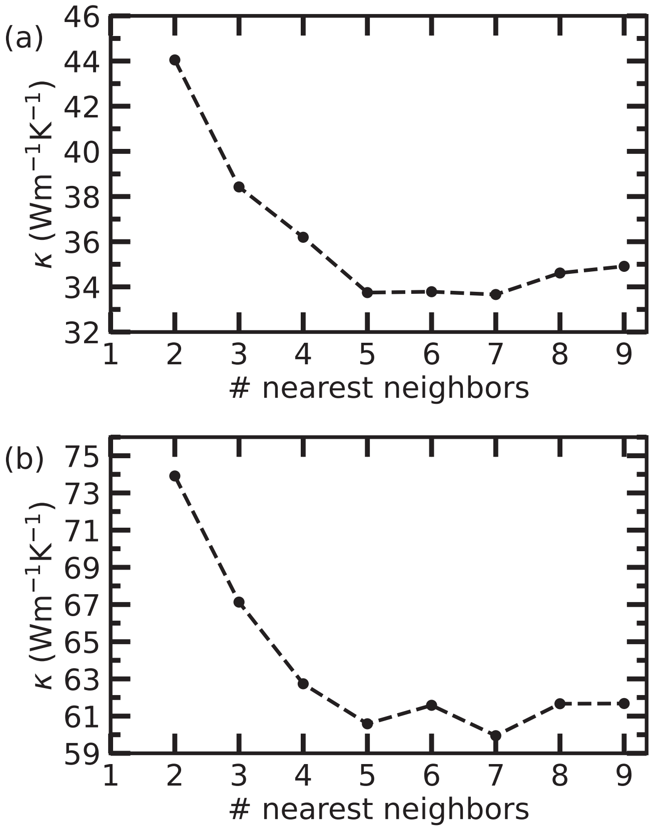

FIG. 11. Convergence of the calculated thermal conductivity in the (a) $\perp c$ direction and (b) $\parallel c$ direction of GeO_2 at 300 K with respect to the number of nearest neighbors included for the generation of third-order force constants. The changes in thermal conductivity evaluated beyond the inclusion of the 5th nearest neighbor is within 2%.

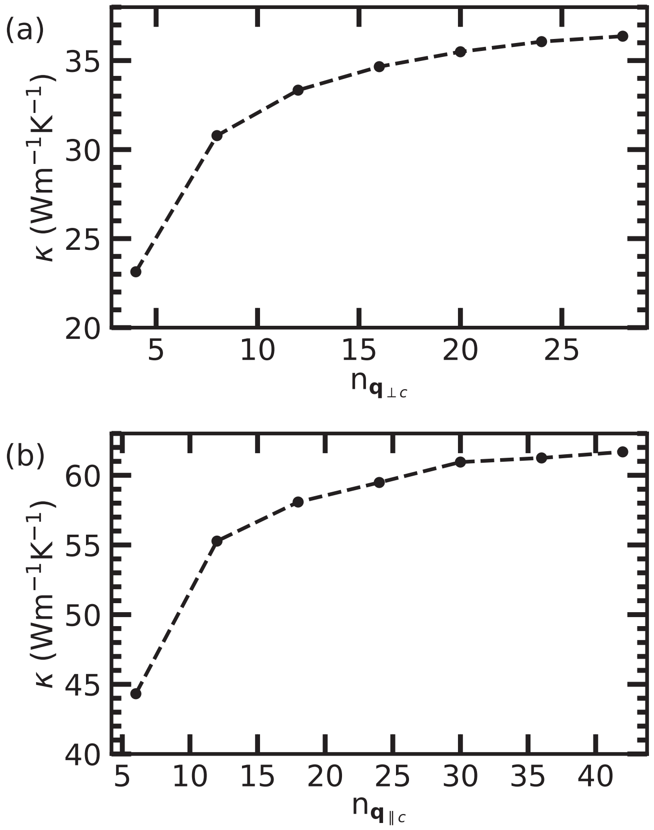

FIG. 12. Convergence of the calculated thermal conductivity in the (a) $\perp c$ direction and (b) $\parallel c$ direction of GeO_2 at 300 K with respect to the grid for solving the phonon BTE. With a sampling of 16 × 16 × 24, the calculated thermal conductivity converges within 3%.

The thermal conductivity is found to be more sensitive to the number of nearest neighbors included. Due to the large increase in the amount of supercells required when increasing the number of nearest neighbors, we performed the test only for GeO_2 at 300 K with 3 × 3 × 3 supercell, considering up to the 9$^{\text{th}}$ nearest neighbor. For the test, the Ge 3*d* electrons are excluded to reduce the computational cost, as the convergence behavior is not expected to be affected. We show the calculated thermal conductivity as a function of the nearest neighbors included in Fig. 11. It can be seen that the nearest neighbor included has a strong effect on the thermal conductivity until the 5th nearest neighbor, but does not further vary by more than 2% when more nearest neighbors are included. Therefore, the 5th nearest neighbor is included to evaluate the third-order force constant in the production calculations in the main text.

Lastly, we test the convergence of the calculated thermal conductivity with respect to the Brillouin zone sampling grid to solve the Boltzmann transport equation. We show the changes in the thermal conductivity in Fig. 12. The calculated thermal conductivity converges quickly beyond a sampling of 12 × 12 × 18, and after reaching 16 × 16 × 24, further increasing the sampling result in changes of the thermal conductivity within 3%. Therefore, we conclude that a grid of 16 × 16 × 24 is sufficient.

Overall, the convergence tests suggest that the parameters we chose in the main text resulted in the calculated thermal conductivity converging within 5%, with the most sensitive parameters being the number of nearest neighbors included and the grid for solving the phonon BTE. This difference is lower than that of the difference compared to experimental measurements, as shown in Fig 4, and also lower than the difference of the calculated data points and the fitted model from Eq. (3). A similar combination of parameters is used in the previous study on GeO_2 [32], and results in a very close value of thermal conductivity at room temperature ($\perp c$: 37 Wm^{-1}K^{-1}, $\parallel c$: 58 Wm^{-1}K^{-1}) compared to our prediction ($\perp c$: 34 Wm^{-1}K^{-1}, $\parallel c$: 58 Wm^{-1}K^{-1}).

---

[1] A. Wang, K. Bushick, N. Pant, W. Lee, X. Zhang, J. Leveillee, F. Giustino, S. Poncé, and E. Kioupakis, Electron mobility of SnO_2 from first principles, Appl. Phys. Lett. **124**, 172103 (2024).

[2] Q. Jiang, X. Zhang, and J. You, SnO_2: A wonderful electron transport layer for perovskite solar cells, Small **14**, 1801154 (2018).

[3] C. G. Fonstad and R. H. Rediker, Electrical properties of high-quality stannic oxide crystals, J. Appl. Phys. **42**, 2911 (1971).

[4] O. Bierwagen and Z. Galazka, The inherent transport anisotropy of rutile tin dioxide (SnO_2) determined by van der Pauw measurements and its consequences for applications, Appl. Phys. Lett. **112**, 092105 (2018).

[5] W. Göpel and K. D. Schierbaum, SnO_2 sensors: Current status and future prospects, Sens. Actuators B **26**, 1 (1995).

[6] S. Das and V. Jayaraman, SnO_2: A comprehensive review on structures and gas sensors, Prog. Mater. Sci. **66**, 112 (2014).

[7] Ç. Kılıç and A. Zunger, Origins of coexistence of conductivity and transparency in SnO_2, Phys. Rev. Lett. **88**, 095501 (2002).

[8] A. Ben-Shalom, L. Kaplan, R. Boxman, S. Goldsmith, and M. Nathan, SnO_2 transparent conductor films produced by filtered vacuum arc deposition, Thin Solid Films **236**, 20 (1993).

[9] Y. Sato, R. Tokumaru, E. Nishimura, P.-k. Song, Y. Shigesato, K. Utsumi, and H. Iigusa, Structural, electrical, and optical properties of transparent conductive In_2O_3–SnO_2 films, J. Vac. Sci. Technol. A **23**, 1167 (2005).

[10] H. Peelaers, E. Kioupakis, and C. G. Van de Walle, Fundamental limits on optical transparency of transparent conducting oxides: Free-carrier absorption in SnO_2, Appl. Phys. Lett. **100**, 011914 (2012).

[11] H. Peelaers, E. Kioupakis, and C. G. Van de Walle, Free-carrier absorption in transparent conducting oxides: Phonon and impurity scattering in SnO_2, Phys. Rev. B **92**, 235201 (2015).

[12] M. Labed, H. J. Jeon, J. H. Park, S. Pearton, and Y. S. Rim, Rutile germanium dioxide: An emerging ultrawide bandgap semiconductor for power device applications–A review, Mater. Today **83**, 513 (2025).

[13] G. Deng, K. Saito, T. Tanaka, M. Arita, and Q. Guo, Pulsed laser deposition growth of ultra-wide bandgap GeO_2 film and its optical properties, Appl. Phys. Lett. **119**, 182101 (2021).

[14] M. S. Rathore, A. Vinod, R. Angalakurthi, A. Pathak, S. K. Thatikonda, and S. R. Nelamarri, Role of oxygen pressure on the structural and photoluminescence properties of pulsed laser deposited GeO_2 thin films, Physica B: Condens. Matter **625**, 413466 (2022).

[15] S. Chae, J. Lee, K. A. Mengle, J. T. Heron, and E. Kioupakis, Rutile GeO_2: An ultrawide-band-gap semiconductor with ambipolar doping, Appl. Phys. Lett. **114**, 102104 (2019).

[16] S. Chae, K. Mengle, K. Bushick, J. Lee, N. Sanders, Z. Deng, Z. Mi, P. F. P. Poudeu, H. Paik, J. T. Heron, and E. Kioupakis, Toward the predictive discovery of ambipolarly dopable ultra-wide-band-gap semiconductors: The case of rutile GeO_2, Appl. Phys. Lett. **118**, 260501 (2021).

[17] K. Bushick, K. A. Mengle, S. Chae, and E. Kioupakis, Electron and hole mobility of rutile GeO_2 from first principles: An ultrawide-bandgap semiconductor for power electronics, Appl. Phys. Lett. **117**, 182104 (2020).

[18] H. Takane and K. Kaneko, High-speed growth of epitaxial rutile GeO_2 thin film on (001) TiO_2 under highly oxygen-rich condition and its structural analysis, ECS Meeting Abstracts **MA2021-02**, 1902 (2021).

[19] H. Takane and K. Kaneko, Establishment of a growth route of crystallized rutile GeO_2 thin film ($\geqslant$1 μm/h) and its structural properties, Appl. Phys. Lett. **119**, 062104 (2021).

[20] S. Chae, L. A. Pressley, H. Paik, J. Gim, D. Werder, B. H. Goodge, L. F. Kourkoutis, R. Hovden, T. M. McQueen, E. Kioupakis, and J. T. Heron, Germanium dioxide: A new rutile substrate for epitaxial film growth, J. Vac. Sci. Technol. A. **40**, 050401 (2022).

[21] A. M. Abed and R. L. Peterson, Effect of post-deposition annealing on crystal structure of RF magnetron sputtered germanium dioxide thin films, J. Vac. Sci. Technol. A **42**, 063403 (2024).

[22] I. Rahaman, B. G. Duersch, H. D. Ellis, M. A. Scarpulla, and K. Fu, Epitaxial growth of rutile GeO_2 via MOCVD, Appl. Phys. Lett. **125**, 102103 (2024).

[23] F. Golbasi, B. Liu, J. Hwang, and F. Akyol, Characteristics of single crystalline rutile GeO_2 film grown on sapphire by chemical vapor deposition with a high growth rate ~2.2 μm/hr, J. Alloys Compd. **1014**, 178591 (2025).

[24] R. Essajai, E. Salmani, M. Bghour, A. Labrag, F. Goumrhar, M. Fahoume, and H. Ez-Zahraouy, Co-, Fe-, Ni-doped and co-doped rutile GeO_2: Insights from ab-initio calculations, Commun. Theor. Phys. **74**, 045701 (2022).

[25] C. A. Niedermeier, K. Ide, T. Katase, H. Hosono, and T. Kamiya, Shallow valence band of rutile GeO_2 and P-type doping, J. Phys. Chem. C **124**, 25721 (2020).

[26] Z. Galazka, R. Blukis, A. Fiedler, S. Bin Anooz, J. Zhang, M. Albrecht, T. Remmele, T. Schulz, D. Klimm, M. Pietsch, A. Kwasniewski, A. Dittmar, S. Ganschow, U. Juda, K. Stolze, M. Suendermann, T. Schroeder, and M. Bickermann, Bulk single crystals and physical properties of rutile GeO_2 for high-power electronics and deep-ultraviolet optoelectronics, Phys. Status Solidi B 2400326.

[27] H. Takane, Y. Ota, T. Wakamatsu, T. Araki, K. Tanaka, and K. Kaneko, Band-gap engineering of rutile-structured $SnO_2 - GeO_2 - SiO_2$ alloy system, Phys. Rev. Mater. **6**, 084604 (2022).

[28] E. Kluth, Y. Nagashima, S. Osawa, Y. Hirose, J. Bläsing, A. Strittmatter, R. Goldhahn, and M. Feneberg, Blue shift of the absorption onset and bandgap bowing in rutile $Ge_xSn_{1-x}O_2$, Appl. Phys. Lett. **125**, 122102 (2024).

[29] Y. Nagashima, M. Fukumoto, M. Tsuchii, Y. Sugisawa, D. Sekiba, T. Hasegawa, and Y. Hirose, Deep ultraviolet transparent electrode: Ta-doped rutile $Sn_{1-x}Ge_xO_2$, Chem. Mater. **34**, 10842 (2022).

[30] F. Liu, N. J. Szymanski, K. Noordhoek, H.-s. Shin, D. Kim, C. J. Bartel, and B. Jalan, Unraveling the growth dynamics of rutile $Sn_{1-x}Ge_xO_2$ using theory and experiment, Nano Lett. **25**, 299 (2025).

[31] Z. Galazka, *Transparent Semiconducting Oxides: Bulk Crystal Growth and Fundamental Properties* (Jenny Stanford Publishing, New York, 2020).

[32] S. Chae, K. A. Mengle, R. Lu, A. Olvera, N. Sanders, J. Lee, P. F. P. Poudeu, J. T. Heron, and E. Kioupakis, Thermal conductivity of rutile germanium dioxide, Appl. Phys. Lett. **117**, 102106 (2020).

[33] V. Palankouski, R. Schultheis, and S. Selberherr, Simulation of power heterojunction bipolar transistors on gallium arsenide, IEEE Trans. Electron Devices **48**, 1264 (2001).

[34] M. Wagner, G. Span, S. Holzer, O. Triebl, T. Grasser, and V. Palankovski, Power output improvement of silicon-germanium thermoelectric generators, ECS Transactions **3**, 1151 (2006).

[35] L. Huang, S. Fan, L. Sang, Y. Mei, L. Ying, B. Zhang, and H. Long, Thermal conductivity and phonon scattering of AlGaN nanofilms by elastic theory and Boltzmann transport equation, Semicond. Sci. Technol. **37**, 055003 (2022).

[36] W. Liu and A. A. Balandin, Temperature dependence of thermal conductivity of $Al_xGa_{1-x}N$ thin films measured by the differential 3ω technique, Appl. Phys. Lett. **85**, 5230 (2004).

[37] K. Strzałkowski, A. Abouais, A. Alaoui-Belghiti, D. Singh, and A. Hajjaji, Alloy disordering effects on the thermal conductivity and energy gap temperature dependence of $Cd_{1-x}Zn_xSe$ ternary crystals grown by the bridgman method, Materials **16**, 3945 (2023).

[38] W. Kohn and L. J. Sham, Self-consistent equations including exchange and correlation effects, Phys. Rev. **140**, A1133 (1965).

[39] P. Hohenberg and W. Kohn, Inhomogeneous electron gas, Phys. Rev. **136**, B864 (1964).

[40] P. Giannozzi, S. Baroni, N. Bonini, M. Calandra, R. Car, C. Cavazzoni, D. Ceresoli, G. L. Chiarotti, M. Cococcioni, I. Dabo *et al.*, QUANTUM ESPRESSO: A modular and open-source software project for quantum simulations of materials, J. Phys.: Condens. Matter **21**, 395502 (2009).

[41] P. Giannozzi, O. Andreussi, T. Brumme, O. Bunau, M. B. Nardelli, M. Calandra, R. Car, C. Cavazzoni, D. Ceresoli, M. Cococcioni *et al.*, Advanced capabilities for materials modelling with QUANTUM ESPRESSO, J. Phys.: Condens. Matter **29**, 465901 (2017).

[42] M. Fuchs and M. Scheffler, *Ab initio* pseudopotentials for electronic structure calculations of poly-atomic systems using density-functional theory, Comput. Phys. Commun. **119**, 67 (1999).

[43] J. P. Perdew and A. Zunger, Self-interaction correction to density-functional approximations for many-electron systems, Phys. Rev. B **23**, 5048 (1981).

[44] D. M. Ceperley and B. J. Alder, Ground state of the electron gas by a stochastic method, Phys. Rev. Lett. **45**, 566 (1980).

[45] S. Baroni, S. de Gironcoli, A. Dal Corso, and P. Giannozzi, Phonons and related crystal properties from density-functional perturbation theory, Rev. Mod. Phys. **73**, 515 (2001).

[46] J. Carrete, B. Vermeersch, A. Katre, A. van Roekeghem, T. Wang, G. K. Madsen, and N. Mingo, almaBTE : A solver of the space–time dependent Boltzmann transport equation for phonons in structured materials, Comput. Phys. Commun. **220**, 351 (2017).

[47] A. Zunger, S.-H. Wei, L. G. Ferreira, and J. E. Bernard, Special quasirandom structures, Phys. Rev. Lett. **65**, 353 (1990).

[48] M. Berglund and M. E. Wieser, Isotopic compositions of the elements 2009 (IUPAC Technical Report), Pure Appl. Chem. **83**, 397 (2011).

[49] W. Li, J. Carrete, N. A. Katcho, and N. Mingo, ShengBTE: A solver of the Boltzmann transport equation for phonons, Comput. Phys. Commun. **185**, 1747 (2014).

[50] T. Lan, C. W. Li, and B. Fultz, Phonon anharmonicity of rutile SnO_2 studied by Raman spectrometry and first principles calculations of the kinematics of phonon-phonon interactions, Phys. Rev. B **86**, 134302 (2012).

[51] A. Kahan, J. W. Goodrum, R. Singh, and S. S. Mitra, Polarized reflectivity spectra of tetragonal GeO_2, J. Appl. Phys. **42**, 4444 (1971).

[52] R. Kaindl, D. M. Többens, S. Penner, T. Bielz, S. Soisuwan, and B. Klötzer, Quantum mechanical calculations of the vibrational spectra of quartz-and rutile-type GeO_2, Phys. Chem. Miner. **39**, 47 (2012).

[53] T. Özer and S. Çabuk, Investigation of structural and mechanical properties of rutile SnO_2, Mater. Res. Express **6**, 085069 (2019).

[54] H. Wang and G. Simmons, Elasticity of some mantle crystal structures: 2. Rutile GeO_2, J. Geophys. Res. **78**, 1262 (1973).

[55] G. Guo, X. Yang, J. Carrete, and W. Li, Revisiting the thermal conductivity of Si, Ge and diamond from first principles: Roles of atomic mass and interatomic potential, J. Phys.: Condens. Matter **33**, 285702 (2021).

[56] See Supplemental Material at http://link.aps.org/supplemental/10.1103/cgkf-djns for tabulated data including calculated thermal conductivities in Figs. 6 and 8. See Readme.txt within the Supplemental Material for details.

[57] N. Mingo, D. A. Stewart, D. A. Broido, L. Lindsay, and W. Li, *Ab initio* thermal transport, in *Length-Scale Dependent Phonon Interactions*, edited by S. L. Shindé and G. P. Srivastava (Springer, New York, 2014), pp. 137–173.